

IUTAM Symposium Wind Waves, 4-8 September 2017, London, UK

Computational Turbulent Shear Flows Over Growing And Non-Growing Wave Groups

S.G. Sajjadi^a, F. Drullion^a, J.C.R. Hunt^b

^a*Embry-Riddle Aeronautical University, Florida, USA.*

^b*University College London, UK.*

Abstract

A high-Reynolds-number second-order stress closure model is used to perform numerical simulations of the wind flow above different groups of waves. It is shown that the group profiles can change as the individual waves grow within its envelop due to the energy transfer between the wind and the group. The focus of this study is the behaviour of the critical-layer and the associated with “cat’s-eye” structures which are centred around the critical height, where the real part of the complex wave speed is equal to the mean flow velocity. It is also shown that the position and size of these structures depend on the wave age and the wave steepness. It is demonstrated that the larger these structures become, the greater disturbance of the wind flow above the wave groups appear. Also, the results obtained here demonstrate how the critical layer structures are asymmetrical over the waves within a group because of the shear driven sheltering effect on the downwind side of the group. The results here complement the general review of wind-wave dynamics by Hunt & Sajjadi [1].

© 2018 The Authors. Published by Elsevier B.V.

Peer-review under responsibility of the scientific committee of the IUTAM Symposium Wind Waves.

Keywords: Type your keywords here, separated by semicolons ;

1. Introduction

Following the review of Hunt and Sajjadi [1], and the points discussed in our earlier paper [13], we perform a numerical simulations of turbulent shear flows over growing and non-growing wave groups, adopting a second-order Reynolds-stress turbulence closure model.

Although the growth and decay of wind generated waves of monochromatic, idealized wave profiles have been extensively studied and are well understood, the interactions and energy transfer between groups of water waves and the ambient wind above them are still not well understood. Experimental, numerical and analytical studies of ocean waves have shown how ocean waves actually travel in groups in which the profiles change as their envelop are

* Corresponding author. Tel.: +0-000-000-0000 ; fax: +0-000-000-0000.

E-mail address: author@institute.xxx

travelling. In this study we consider how consider in particular how ocean wave groups grow through their dynamical interaction with turbulent wind shear over the waves.

We focus our attention on the region around the height where the real part of the complex wave speed is equal to the mean flow velocity, i.e. when $U(z_c) = c_r$, where c_r is the real part of the wave speed. This region, namely the “critical layer”, whose thickness is z_c , where closed streamlines (namely cat’s-eye) develop, is the central point in Miles’ theory [2] and Lighthill’s interpretation of growth of waves [3]. Miles considered the limit as the complex wave speed, c_i , tends to zero, and in his subsequent analysis he assumed the complex part of the waves is identically zero. He argued that in this limit there is a finite positive drag over the waves and the energy-transfer rate is only dependent on the curvature of the velocity profile $U(z_c)$ at the critical height $z = z_c$. Furthermore, he only considered steady monochromatic waves of small steepness which were of the order 0.01. But, if the waves do grow or decay, the amplitude of waves must vary in time [13], i.e. $a(t) = a_0 e^{kc_i t}$, where a_0 is the initial amplitude and k is the wavenumber.

It has been shown by [12], that as the cat’s-eye become larger the flow over the waves become more disturbed. Also as the wave age (i.e. U/U_*) increases, the elevation of the cat’s-eyes exceed the thickness ℓ of the inner surface layer i.e. $z_c > \ell$, then there is a strong reverse flow below the critical layer which affects the surface drag, and thus the energy-transfer rate, β . This is consistent with recent findings [12, 15] who showed that as waves steepen then β increases. But for monochromatic waves, z_c is symmetrically placed over the waves [12, 5]. However, for wave groups the critical layer becomes more asymmetrical particularly as waves grow [14].

2. Governing equations

The air flow with density ρ_a and kinematic viscosity ν_a over the group of waves is governed by the incompressible Reynolds averaged Navier-Stokes equations:

$$\frac{\partial U_i}{\partial x_i} = 0 \quad (1)$$

$$\frac{DU_i}{Dt} = -\frac{1}{\rho_a} \frac{\partial P}{\partial x_i} + \frac{\partial}{\partial x_j} \left[\nu_a \left(\frac{\partial U_i}{\partial x_j} + \frac{\partial U_j}{\partial x_i} \right) - \overline{u'_i u'_j} \right] \quad (2)$$

where U_i is the mean velocity component in the x_i -direction, P is the mean pressure, $\overline{u'_i u'_j}$ is the Reynolds-averaged stress correlation and t is time.

A model for the Reynolds-averaged stress correlations is needed to close equation (2). A rational approach for providing a model for $\overline{u'_i u'_j}$ in equation (2) relies on its transport equation, which may be written in the following form

$$\frac{D\overline{u'_i u'_j}}{Dt} = P_{ij} + \Pi_{ij} - \varepsilon_{ij} + d_{ij} \quad (3)$$

where $P_{ij} = -(\overline{u'_i u'_k} \partial U_j / \partial x_k + \overline{u'_j u'_k} \partial U_i / \partial x_k)$ is the production term, Π_{ij} represents the velocity-pressure gradient correlation, ε_{ij} the viscous dissipation, and d_{ij} represents diffusion by both molecular viscosity and the triple velocity moments. On the left-hand side of (3), the stress convection, and the production term are both exact and require no further modelling. However, all other terms contain further unknowns which must be modelled. For this we adopt a high-Reynolds-number turbulence model [6]. In this model, the pressure correlation Π_{ij} is decomposed into a redistributive part, ϕ_{ij}^* , and a non-redistributive part by

$$\Pi_{ij} \equiv -\frac{1}{\rho_a} \left(\overline{u'_i \frac{\partial p'}{\partial x_j}} + \overline{u'_j \frac{\partial p'}{\partial x_i}} \right) = \phi_{ij}^* + \frac{\overline{u'_i u'_j}}{2K} d_{kk}^p \quad (4)$$

where $d_{kk}^p = -(1/\rho_a) \partial \overline{u'_k p'} / \partial x_k$ represents the pressure diffusion of the turbulent kinetic energy $K = \frac{1}{2} \overline{u'_i u'_i}$. The model employed for the redistributive part of the pressure correlation, ϕ_{ij}^* , is based on the cubic realizable form derived by Fu [7]. The dissipation ε_{ij} is modelled as

$$\varepsilon_{ij} = \left(1 - A^{1/2} \right) \frac{\varepsilon}{K} \overline{u'_i u'_j} + \frac{2}{3} \varepsilon \delta_{ij} \quad (5)$$

where $A = 1 - 9/8(A_2 - A_3)$, $A_2 = a_{ij}a_{ij}$, $A_3 = a_{ij}a_{jk}a_{ki}$ and $a_{ij} = \overline{u'_i u'_j} / K - \frac{2}{3}\delta_{ij}$. This model is very similar to the form adopted in other high-Reynolds-number flows, see for example Gibson & Launder [8]. In (5) The dissipation rate ε is derived through the solution of its own transport equation:

$$\begin{aligned} \frac{D\varepsilon}{Dt} = c_{\varepsilon 1} \frac{\varepsilon P_{kk}}{2K} - c_{\varepsilon 2} \frac{\varepsilon^2}{K} + \frac{\partial}{\partial x_l} \left[\left(\nu_a \delta_{lk} + c_{\varepsilon} \overline{u'_l u'_k} \frac{K}{\varepsilon} \right) \frac{\partial \varepsilon}{\partial x_k} \right] \\ + c_{\varepsilon 3} A^{1/2} (1 - A) \frac{\varepsilon}{\sqrt{K}} \overline{u'_i u'_j} \frac{\partial A}{\partial x_i} \frac{\partial}{\partial x_j} \left(\frac{K^{3/2} A^{1/2}}{\varepsilon} \right) \end{aligned} \quad (6)$$

with coefficients

$$c_{\varepsilon 1} = 1.0, \quad c_{\varepsilon 2} = 1.92/(1 + 0.7A_d A_2^{1/2}), \quad A_d = \max(0.2, A), \quad c_{\varepsilon 3} = 1.0, \quad c_{\varepsilon} = 0.18$$

The only remaining term in the stress transport equations is the diffusion term

$$d_{ij} = \frac{\partial}{\partial x_k} \left(\nu_a \frac{\partial \overline{u'_i u'_j}}{\partial x_k} - \overline{u'_i u'_j u'_k} \right) \quad (7)$$

The viscous diffusion is, of course exact, and the triple correlations are modelled via the proposal of Hanjalic & Launder [9] proposal

$$\overline{u'_i u'_j u'_k} = -c_s \frac{K}{\varepsilon} \left[\overline{u'_i u'_l} \frac{\partial \overline{u'_j u'_k}}{\partial x_l} + \overline{u'_j u'_l} \frac{\partial \overline{u'_i u'_k}}{\partial x_l} + \overline{u'_k u'_l} \frac{\partial \overline{u'_i u'_j}}{\partial x_l} \right] \quad (8)$$

where $c_s = 0.11$.

3. Numerical scheme

The finite volume method is used to solve the governing equations. The volumes are non-orthogonal and collocated such that all flow variables are stored at the centered of the cells. The numerical scheme uses a pressure based solver [10]. A first order forward discretization in time is used, and the convective fluxes are approximated with the higher-order upstream-weighted scheme, QUICK of Leonard [11]. The pressure and diffusive fluxes are discretized using a central difference operator. The finite volume method and the chosen discretizations lead to penta-diagonal system solved using a tri-diagonal, matrix algorithm (TDMA). The discretization is proceeded by a transformation of the Cartesian coordinates of the governing equations to the non-orthogonal coordinates ξ and ζ using the Jacobian transformation matrix. The transport equation for any scalar property Φ many be expressed in non-orthogonal direction as

$$\begin{aligned} \underbrace{\frac{\partial}{\partial t} (J \rho_a \Phi)}_{\text{transient term}} + \underbrace{\frac{\partial}{\partial \xi} (\rho_a U^{(\xi, \zeta)} \Phi) + \frac{\partial}{\partial \zeta} (\rho_a W^{(\xi, \zeta)} \Phi)}_{\text{convection}} \\ + \underbrace{\frac{\partial}{\partial \xi} \left(\alpha_\Phi J \frac{\partial \Phi}{\partial \xi} \right) + \frac{\partial}{\partial \zeta} \left(\beta_\Phi J \frac{\partial \Phi}{\partial \zeta} \right)}_{\text{diffusion}} = \underbrace{JS_\Phi}_{\text{source}} \end{aligned} \quad (9)$$

where $U^{(\xi, \zeta)} = Uz_\zeta - Wx_\zeta$ and $W^{(\xi, \zeta)} = Wx_\xi - Uz_\xi$ are contravariant velocity components, J is the Jacobian of the transformation, S_Φ is the source term including diffusive terms, pressure terms in the momentum equation, $\alpha_\Phi = \Gamma_\Phi(x_\zeta^2 + z_\zeta^2)$, $\beta_\Phi = \Gamma_\Phi(x_\xi^2 + z_\xi^2)$, where Γ_Φ is isotropic diffusivity, and the subscripts ξ, ζ denote partial differentiations. The mesh covering the computational domain contains 200×100 nodes and extends over six wavelengths in horizontal direction and two wavelength in the vertical direction. As can be seen from figure 1, it is refined near the water surface in order to capture the steep gradients which are inherently present there.

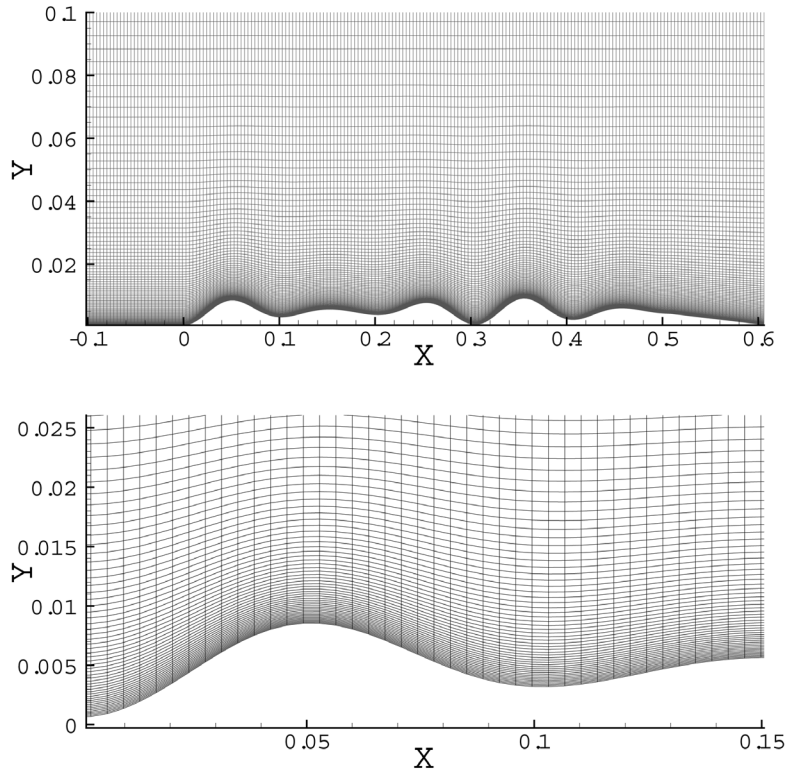


Fig. 1. Computational mesh adopted. Top is the entire region, bottom zoom of a region showing the compression of grids near the surface.

4. Problem set up and wave group construction

We consider groups of waves composed by superposition of three cosine waves (see equation 11 below). The groups are traveling in deep water at the speed $c_r = \frac{1}{2} \sqrt{\frac{g}{k}}$ and a wind whose mean velocity is assumed to be logarithmic is blowing above them. At the height of one wavelength above the surface of the wave, the wind velocity is imposed to be U_λ . The turbulent flow has a mean velocity profile $U(\zeta) = U_1 \ln(\zeta/\zeta_0)$, $U_1 \equiv U_*/\kappa$, U_* being the friction velocity, κ being the von Kármán's constant, and ζ_0 is the surface roughness. Note that, ξ and ζ are the wave-following coordinates, given by the following transformation

$$x = \xi, \quad z = \zeta + h(\xi, \zeta) \quad (10)$$

where $h = h(\xi, \zeta)$ maps $z = h_0$ onto $\zeta = 0$ and is evanescent for $k\zeta \uparrow \infty$ but is otherwise arbitrary. The computational domain is taken to six wavelengths horizontally and two wavelengths vertically. The groups only extend over four wavelengths (from $x = 0$ to $x = 4\lambda$) and are surrounded by a flat surface. The latter ensures the periodicity in boundary conditions in the x -direction. In our simulations, the frame of reference is traveling with the group. The initial wave group profile is given by:

$$h_0 = a[\cos(k\mathcal{X}) + \epsilon_1 \cos(k_1\mathcal{X}) + \epsilon_2 \cos(k_2\mathcal{X})] \quad (11)$$

where a is the initial wave amplitude k is the wave number, $k_1 = 1 + \sqrt{2}ak$ and $k_2 = 1 - \sqrt{2}ak$ and where $\mathcal{X} = \xi - c_r t$.

5. Boundary conditions

A strictly horizontal velocity $U = U_\lambda - \frac{c_r}{2}$ is imposed at the top of the computational domain, taking into account the fact that the frame of reference is moving with the waves at the speed $\frac{c_r}{2}$.

At the bottom of the domain, the mean velocity components match the wave orbital velocities. The orbital velocities for $0 \leq x \leq 4\lambda$, are given by

$$\begin{aligned} u &= -c_g a k [\cos(kx) + \epsilon_1 k_1 \cos(k_1 x) + \epsilon_2 k_2 \cos(k_2 x)] - c_g \\ v &= -c_g a k [\sin(kx) + \epsilon_1 k_1 \sin(k_1 x) + \epsilon_2 k_2 \sin(k_2 x)] \end{aligned}$$

Note that, for the flat surfaces surrounding the group portion on the south boundary, namely when $x < 0$ and $x > 4\lambda$, we impose the conditions $u = -c_g$ and $v = 0$. In the streamwise direction, periodic boundary conditions are imposed on all the mean variables and the turbulent stresses together with the turbulent dissipation rate. At the top and the bottom of the computational domain the boundary conditions imposed on the stresses and the dissipation rate are the same as the one used in [12]. The boundary conditions for stresses and dissipation rate is taken from our earlier paper [12].

6. Results

In this paper we report computations of turbulent flow over two groups both in a frame of reference moving with the wave, namely *group1* and *group2*. For both groups, the initial amplitude of the main cosine wave is $a(0) = 0.0025$ m and its wavelength is $\lambda = 0.1016$ m. Here, $(\epsilon_i)_{1,2}$ for *group1* and *group2* are respectively: $(\epsilon_1 = 0.2, \epsilon_2 = 0.1)$ and $(\epsilon_1 = 0.25, \epsilon_2 = 0.5)$.

Note that, for all the diagrams, the vertical axis has been normalized using the fundamental wave number k .

6.1. Non-growing groups

We first consider the influence of the wave age on the cat's-eye structures over non-growing groups for the following three wave ages: $c_r/U_* = 1$, $c_r/U_* = 3.5$, and $c_r/U_* = 7$. Figures 2 and 3 show the contour plots of the stream function for respectively *group1* and *group2* as a function for three wave ages $c_r/U_* = 1, 3.5$ and 7 . As it can be seen from these figures, at lowest value of c_r/U_* cat's-eye structures are formed downstream of the steepest waves in the group. As the wave age increases to 3.5 , we note that new weaker cat's-eye structures appear in the lee of the waves where they were not previously present, the pre-existing structures increase in size and their center slightly shift toward the peak of the wave behind of them, the cat's-eye structures also slightly lift up from the surface of the wave. At $c_r/U_* = 7$ the cat's-eye become stronger and move further over the peak of the waves in the group. At the largest value of the wave age we can observe a maximum disturbance of the mean flow above the waves, the critical height, passing through the center of the cat's-eye structures is lifted above the crests of the waves.

6.2. Growing groups

We next consider the case where group of waves for which the initial profile as well as the lower boundary condition can evolve under the influence of the turbulent wind flow above the wave. For the growing groups, the computational mesh is regenerated every 50 time steps, where each time step consists of 500 iterations and is increased as the waves become steeper. All the variables are then interpolated/extrapolated onto the new mesh. The growth factor for each wave within the group is $e^{Kc_{it}}$, where K can be taken to be k, k_1 or k_2 and

$$c_i = 8c_g a / \lambda.$$

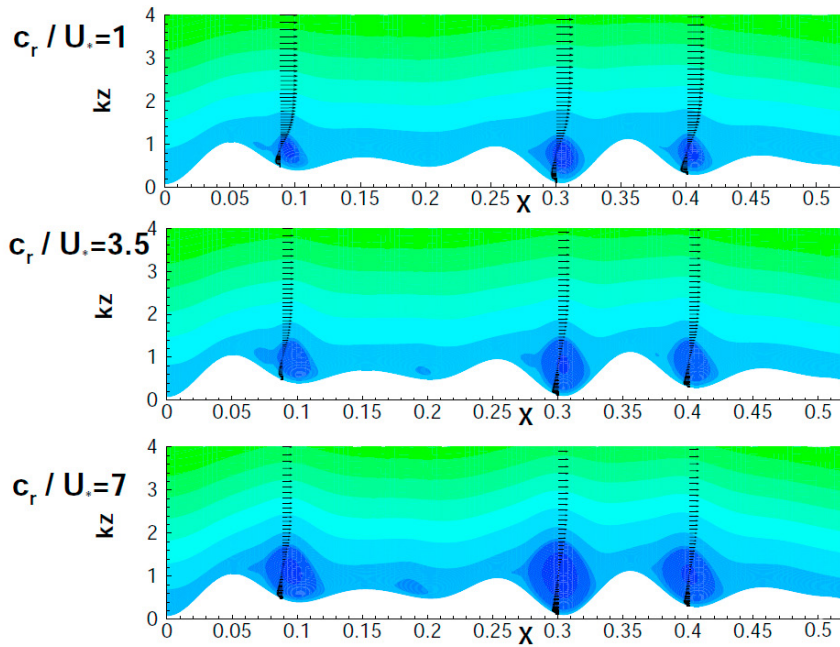


Fig. 2. Contour plots and velocity vector field of the stream function over *group1* wave for three values of the wave age $c_r/U_* = 1$ (top); 3.5 (middle), and 7 (bottom).

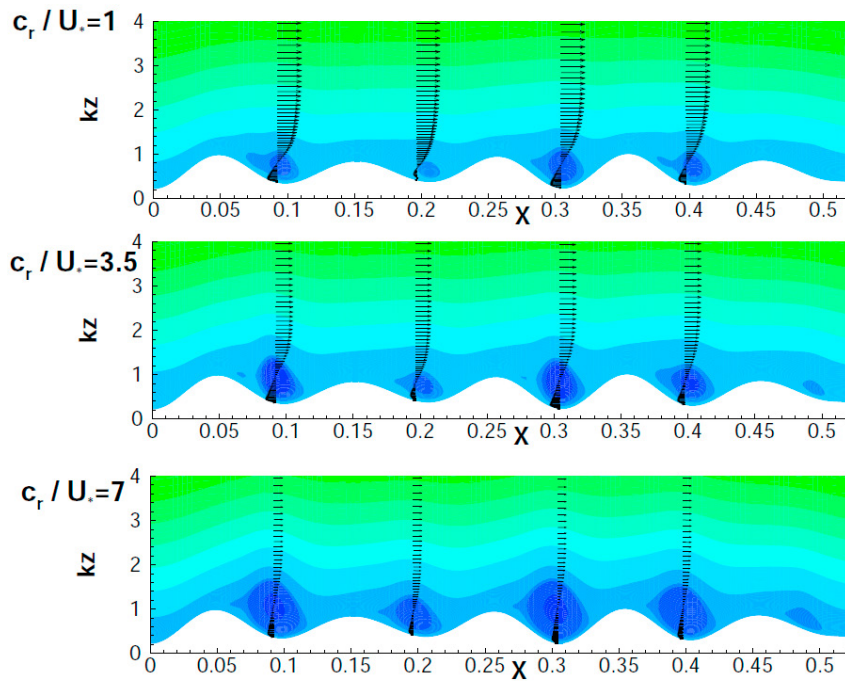


Fig. 3. Contour plots of stream function and velocity vector field over *group2* wave for three values of the wave age $c_r/U_* = 1$ (top); 3.5 (middle), and 7 (bottom).

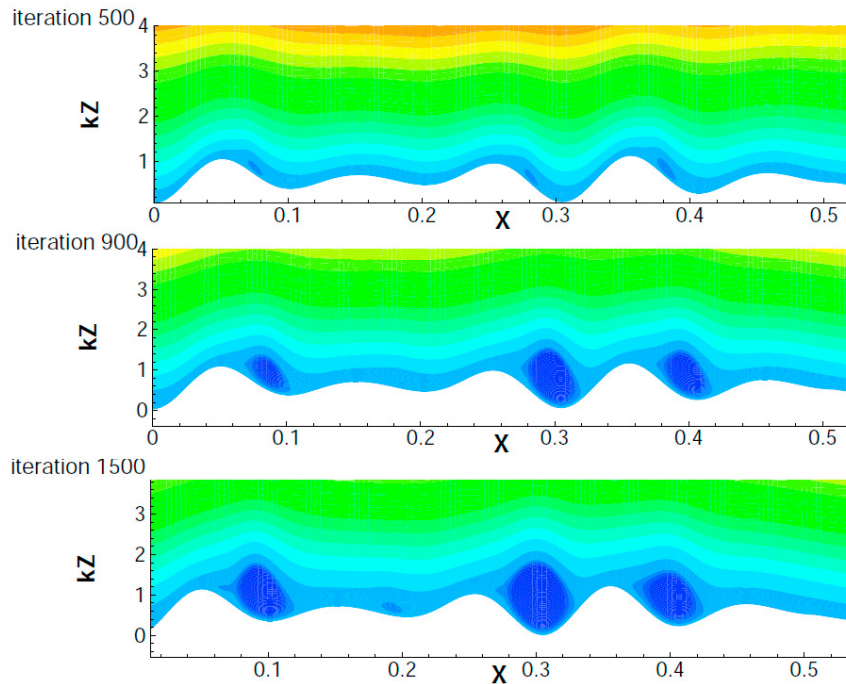


Fig. 4. Contour plots of stream function over growing *group1* wave for a single value of the wave age $c_r/U_* = 5.75$. Steepest wave is depicted at the bottom.

This choice of the complex wave celerity is chosen such that it yields a similar magnitude as that used in our earlier contribution [13]. A more physical expression may be deduced from parameterization expression for the energy-transfer rate from wind to waves, see [15].

In figure 4, we display the result of simulations for *group2* growing under the influence of the surrounding wind, for one fixed value of the wave age $c_r/U_* = 5.75$. As it can be seen, when the wave steepens, the cat's-eye structures are formed in the lee of the waves in the group. As the waves grow so do the cat's-eyes, similarly to our other computations for monochromatic waves and bimodal Stokes waves [12] (see also Sullivan *et al.* [5]). Note also how the critical height rises higher above the surface of the waves. It is also evident that the flow become more asymmetrical. In the air flow over the upwind part of the group where $c_i > 0$, the net drag increases. This increases the general flow over the whole group even though $c_i < 0$ on the downwind side of the group.

7. Conclusion

In this study a high-Reynolds-number stress model is used to simulate the turbulent wind flow above growing and non-growing groups of waves for different ratios of wind speed to turbulence intensity, i.e. 'wave age'. Our simulations show that both the height of the critical layer, as well as the shape and positions of the cat's-eye structures, form over groups of waves dependent on the wave age as previously demonstrated for monochromatic and Stokes waves with the same computational model [12]. As the wave age (c_r/U_*) increases the cat's-eye becomes larger. Consequently the critical layers are elevated higher over the waves and also become significantly asymmetrical, with a stronger reverse flow below them. This asymmetry causes the critical layer height to be lower over the downwind part of the group in accordance with the conclusion drawn from earlier results [13, 14]. Thus, the positive growth of the individual waves on the upwind part of the wave group exceeds the negative growth on the downwind part. Hence, the effect of grouping on the critical layer produces a net horizontal force on the waves, in addition to the sheltering effect. This explains

why the heuristic combinations of inviscid modelling of cat's-eye dynamics (as in Janssen [16]) and inertial-shear stress modelling provide practical methods for wind generated waves.

References

1. J.C.R. Hunt and S.G. Sajjadi, Mechanisms and modelling of wind driven waves, *Proc. Symposium Wind Waves*, 4-8 September 2017, London, UK.
2. J.W. Miles, On the generation of surface waves by shear flows, *J. Fluid Mech.*, **3**, 185, 1957.
3. M.J. Lighthill, Physical interpretation of the theory of wind generated waves, *J. Fluid Mech.* **14**, 385–398, 1962.
4. F. Drullion, & S.G. Sajjadi, Interaction of wind with surface water waves, *Neural, Parallel, and Sci. Comp.* **22**, 303–314, 2014.
5. P.P. Sullivan, J.C. McWilliams & C.H. Moeng, Simulation of turbulent flow over idealized water waves, *J. Fluid Mech.*, **404**, 47–85, 2000.
6. S.G. Sajjadi, T.J. Craft, Y. Feng, A numerical study of turbulent flow over a two-dimensional hill, *Int. J. Numer. Meth. Fl.*, **35**, 1, 2001.
7. S. Fu, B.E. Launder and D.P. Tselepidakis, Accommodating the effects of high strain rates in modelling the pressure-strain correlation, *Rep. No. TFD/87/5*, Mechanical Engineering Department, UMIST, 1987.
8. M.M. Gibson and B.E. Launder, Ground effects on pressure fluctuations in the atmospheric boundary layer, *J. Fluid Mech.*, **86**, 491, 1978.
9. K. Hanjalic and B.E. Launder, A Reynolds stress model of turbulence and its application to thin shear flows, *J. Fluid Mech.*, **52**, 609, 1972.
10. S.V. Patankar, *Numerical Heat Transfer and Fluid Flow*, Taylor & Francis, 1980.
11. B.P. Leonard, A stable and accurate convective modelling procedure based on quadratic upstream interpolation, *Comp. Maths. Appl. Mech. Eng.*, **19**, 59, 1979.
12. S.G. Sajjadi and F. Drullion, Numerical study of Turbulent flow over Growing Monochromatic and Stokes waves, *Adv. Appl. Fluid Mech.*, **19**, 47, 2016.
13. S.G. Sajjadi, J.C.R. Hunt, F. Drullion, Asymptotic Multi-Layer Analysis of Wind Over Unsteady Monochromatic Surface Waves, *Journal of Engineering Mathematics*, **84**, 73, 2014.
14. S.G. Sajjadi, J.C.R. Hunt, F. Drullion, Growth of unsteady wave groups by shear flows, *Proc. of IMA Conference on Turbulence, Waves and Mixing, Kings College Cambridge, U.K., July 2016*, 79–84, 2016.
15. S.G. Sajjadi, J.C.R. Hunt, and F. Drullion. Turbulent shear flows over unsteady ideal and non-ideal water waves. To appear in *J. Fluid Mech.*, 2017.
16. P. A.E.M. Janssen and J-R Bidlot. Progress in operational wave forecasting. *Proc. IUTAM Symposium Wind Waves*, 4-8 September 2017, London, UK.